Underwater acoustic wave generation by filamentation of terawatt ultrashort laser pulses

Vytautas Jukna,[1,*] Amélie Jarnac,[1] Carles Milián,[2] Yohann Brelet,[1] Jérôme Carbonnel,[1] Yves-Bernard André,[1] Régine Guillermin,[3] Jean-Pierre Sessarego,[3] Dominique Fattaccioli,[4] André Mysyrowicz,[1] Arnaud Couairon,[2] and Aurélien Houard[1]

[1] *LOA, ENSTA ParisTech, CNRS, École Polytechnique, Université Paris Saclay, F-91762 Palaiseau cedex, France*
[2] *Centre de Physique Théorique, École polytechnique, CNRS, Université Paris-Saclay, F-91128 Palaiseau, France*
[3] *Laboratoire de Mécanique et d'Acoustique, CNRS - UPR 7051, 4 impasse Nikola Tesla, CS 40006, 13453 Marseille Cedex 13*
[4] *DGA Techniques Navales, Toulon, France*

Acoustic signals generated by filamentation of ultrashort TW laser pulses in water are characterized experimentally. Measurements reveal a strong influence of input pulse duration on the shape and intensity of the acoustic wave. Numerical simulations of the laser pulse nonlinear propagation and the subsequent water hydrodynamics and acoustic wave generation show that the strong acoustic emission is related to the mechanism of superfilamention in water. The elongated shape of the plasma volume where energy is deposited drives the far-field profile of the acoustic signal, which takes the form of a radially directed pressure wave with a single oscillation and a very broad spectrum.

PACS numbers: 42.65.Jx, 43.30.+m, 47.40.-x

I. INTRODUCTION

When a compressible liquid submitted to external forces ruptures violently, cavitation occurs and nucleates bubbles that undergo subsequent implosion and oscillations driven by the external fluid pressure in the surrounding liquid. An acoustic signal is released from the bubble implosion. Cavitation and acoustic wave generation can be a phenomenon to avoid or in contrast, a desired effect provided a certain degree of control can be reached. For instance, cavitation is well known to induce damage on ship propellers, but cavitation-induced high-velocity jets and high pressure acoustic wave in water allow snapping shrimps to stun or kill prey animals [1]. Not only in the natural world but also for numerous applications, from chemical engineering, biomedical ultrasound imaging, to mechanical optical cleaning [2], internal combustion engine efficiency, and interface science [3], would it be desirable to control cavitation and subsequently pressure wave release.

Laser-induced energy deposition in water and effects following optical breakdown have been investigated for the past decades (see [4] for recent findings). Laser induced cavitation in water was discovered in the early sixties [5, 6] and has been the subject of continued interest as it was rapidly recognized that the development of laser-induced acoustic sources in water could open up new possibilities for underwater communications, for high resolution imaging, tomography and fast characterization of marine environment with the aim of exploiting sea resources, or for remote acoustic control of submerged instruments [7]. The first experiments were performed with long pulse laser sources, leading to a slow heating of water followed by thermal expansion and emission of an acoustic wave [8, 9]. The conversion efficiencies from light to the acoustic signal was however reported to be enhanced with nanosecond laser pulses, leading to optical breakdown, rapid heating of the focal volume producing pressures in the gigapascal range and explosive expansion followed by the emission of a shock wave [10–12]. Femtosecond laser pulses open up new possibilities in this field as they were recently shown to lead to ultrabroad acoustic signals [13]. The nonlinear propagation of femtosecond laser pulses in gases or liquids leads to light-plasma filaments, where the laser beam shrinks upon itself due to the Kerr nonlinearity, to reach intensity levels that exceed the threshold for optical field ionization [14]. This high intensity can be sustained over extended distances and the filament itself can be generated remotely, adding to the potential flexibility in tuning laser-induced acoustic sources. The dynamics of femtosecond filamentation in water and its various properties has been investigated thoroughly in the past decade [15–21], however only a few investigations focus on the potential of filaments for cavitation or acoustic wave generation [12, 22–27]. In particular Potemkin et al. demonstrated enhancement of the acoustic signal amplitude with an increase in the length of the focal region [28].

In this paper, we present investigations on acoustic signals generated by ultrashort laser pulse filamentation. Acoustic measurements were done utilizing femtosecond and picosecond laser pulses with energies of tens to hundreds of milli-Joules as sources of acoustic signals. Numerical simulations are performed for understanding the

* vytautas.jukna@ensta-paristech.fr

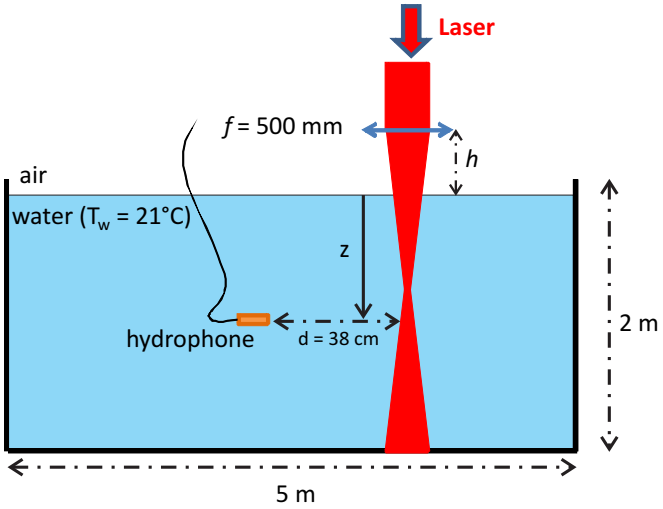


FIG. 1. Experimental setup for generation of acoustic waves with a laser beam and recording them with a hydrophone. h is the distance between the surface of water and the lens while z defines the direction of hydrophone displacement for spatio-temporal acoustic wave analysis.

nonlinear propagation of the laser beam through water, the subsequent hydrodynamic expansion of the focal volume and the propagation of the generated acoustic signal. The numerical simulations are divided into three stages discriminated by the duration of the process: (i) nonlinear propagation of the beam and laser pulse energy deposition into water, (ii) laser-induced nonlinear hydrodynamics and shock-wave formation, (iii) propagation of the acoustic wave to the hydrophone. Acoustic signals recorded at distance from the filament exhibit signatures of the focal volume shape. Our numerical simulations show that a nonsymmetrical acoustic signal arising in conditions for superfilamentation can be interpreted as a manifestation of the shape of the focal volume, which depends on the laser pulse energy and focusing geometry. Loose focusing leads to cylindrical focal regions whereas an increase of the numerical aperture leads to a conically-shaped and shorter focal volume. Ability to dynamically control the directivity of the acoustic sources is important for underwater detection and communications.

II. EXPERIMENTAL SETUP AND RESULTS

The experiment was performed by using a Ti:Sapphire laser with central wavelength of 800 nm, Fourier limited pulse duration of 50 fs and pulse energy of 290 mJ. The beam was focused with a 50 cm lens into a large water tank (Fig. 1). The lens was placed at a height h above the surface of water. The initial beam diameter (FWHM) on the lens was 35 mm, therefore the numerical aperture was NA=0.07. The pulse duration was changed from 0.25 ps to 5 ps by imposing a linear positive chirp on the 50 fs pulse. To register the acoustic waves emitted by

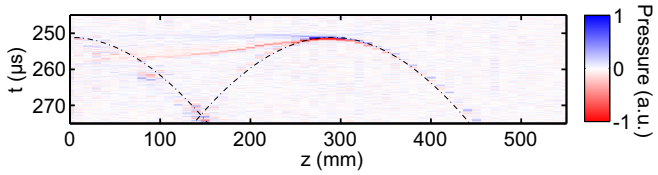


FIG. 2. Typical acoustic wave profile registered by a hydrophone. The focusing lens was 30 cm above the surface of water and the pulse duration was 5 ps. The two dashed curves represent the profiles of the two spherical acoustic waves emitted from point sources located at the depths $z = 0$ and 297 mm (corresponding to the position of the top of the hyperbolic branches). These locations clearly correspond to the water tank surface and to the laser focal region, respectively.

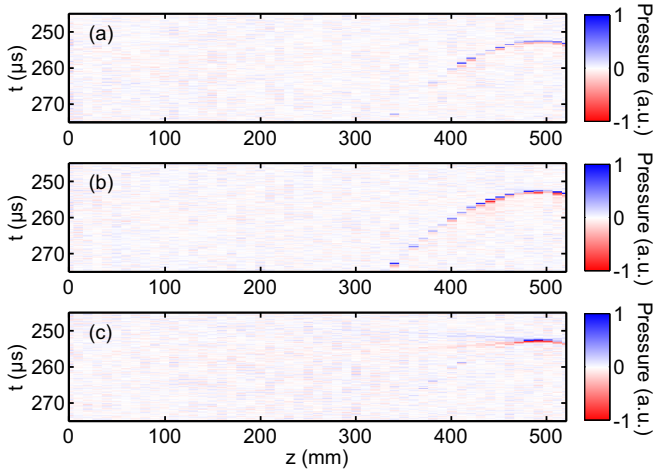


FIG. 3. Comparison of amplitude profiles for the acoustic waves generated by 290 mJ laser pulses with initial duration of (a) 0.25 ps, (b) 0.5 ps, and (c) 5 ps. The lens was positioned at $h = 13$ cm above the surface of water corresponding to a focus depth of $z_0 \sim 500$ mm. Acoustic waves are registered by moving the hydrophone along a vertical axis at distance $d = 38$ cm from the laser propagation axis.

expansion of the focal volume, a very broad band needle hydrophone (flat at ± 4 dB on the band 200 kHz - 15 MHz) was inserted into water at the separation distance $d = 38$ cm away from the propagation axis of the laser beam. The spatial-temporal profiles of the acoustic waves were mapped by varying the immersion depth z of the hydrophone, keeping constant the separation distance d and the focusing geometry, and by recording for each depth the acoustic signal reaching the hydrophone after a laser shot. Figure 2 shows typical measurements. A spherical acoustic wave emitted from a point source located at z_0 is expected to reach the hydrophone at a depth z after a delay $t = \sqrt{d^2 + (z - z_0)^2}/c_s$, where $c_s = 1487$ m/s denotes the speed of sound in water under normal conditions. In other words, the mapped profile when the focus of the lens is located at z_0 should be a hyperbolic branch, centered at z_0, as shown by the dashed curves in Fig. 2. However, our measurements

show additional features. A conical (V-shaped) profile is clearly visible as two branches, representing the positive and negative peaks in the acoustic signal intersecting at the emission point (top of the most visible hyperbolic branch at $z_0 = 270$ mm) corresponding to the focus of the lens, where a maximum in signal amplitude is observed. As will be shown below, several regions of the focal volume contribute to the acoustic signal: In addition to the quasi point source at the focus where the plasma density reaches $\sim 10^{22}$ m^{-3}, multiple filamentation occurs in the vicinity of the focus in an extended focal volume, featured by focusing conditions, and is responsible for the V-shaped acoustic branches. In this particular case there is another source of acoustic waves located at the surface of water, whose origin is not identified in this work but presumably it comes from floating impurities in the water tank. In the measurements discussed below, we moved the focusing lens closer (separation of h = 13 cm) to the surface of water to prevent interference of this acoustic wave generated at the surface of water with acoustic waves generated in the bulk.

We analyzed acoustic wave generation by filamentation with pulses of different initial pulse durations. Figure 3 shows a comparison of acoustic wave profiles generated with pulse durations from 0.25 to 5 ps. The acoustic waves are plotted with the same colormap for possible relative amplitude comparability. Our measurements revealed that higher amplitudes of acoustic waves tend to be obtained with longer pulse durations when the laser energy is kept constant. In addition the profiles corresponding to the shortest pulse durations (0.25 ps, 0.5 ps) exhibit a single branch as in the case of a point source emitting a spherical wave. The amplitude profile of the acoustic wave obtained with the longer pulse (5 ps), exhibits the additional V-shaped branches with amplitudes even larger than generated with shorter pulse durations.

III. NUMERICAL SIMULATIONS OF LASER ENERGY DEPOSITION

Three different tools were used for numerical simulations of the nonlinear pulse propagation, nonlinear hydrodynamics and generation of the acoustic wave, and its propagation to the hydrophone. Nonlinear propagation of the laser pulse was simulated by means of the code developed for investigating superfilamentation, beam symmetrization in air, and filamentation of large beams from orbit [29–31], which resolves a unidirectional envelope propagation equation describing diffraction, the optical Kerr effect, plasma induced effects including plasma defocusing and nonlinear losses due to its generation by multiphoton and by avalanche ionization (see Appendix A). Our numerical scheme (see [32] for details) was upgraded to accommodate beams with high numerical aperture propagating through nonlinear media. A coordinate transformation proposed by Sziklas and Siegman [33] was implemented, allowing us to easily treat the fast oscillating spatial phase. Our model assumes a fixed Gaussian pulse profile over the whole propagation length. This assumption, associated with a preliminary mapping between peak intensity and electron density through the ionization model allows us to perform (2+1)D simulations with the highly demanding resolution required by our focusing geometry and relatively high pulse energy. With these new features, the code was used to simulate filamentation in water and checked to fairly reproduce experimental findings which will be discussed later in the text. The assumption of a fixed Gaussian pulse shape slightly overestimates energy losses, however the model provides a glimpse in the physics behind laser energy deposition for different input beam conditions.

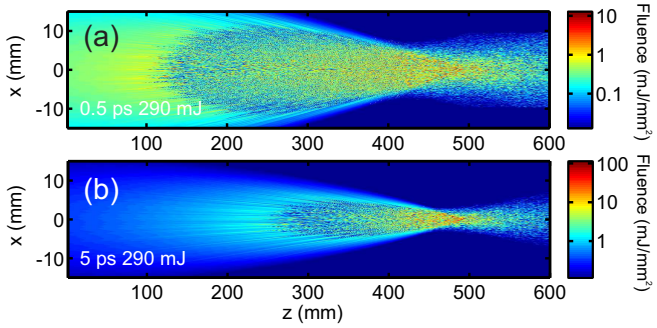


FIG. 4. Fluence profiles (cross section along a single transverse dimension x) for nonlinear propagation of laser pulses in water. The focus of the lens is at $z = 488$ mm. Input pulse energy 290 mJ. Pulse duration: (a) 0.5 ps; (b) 5ps. Maximum fluence values are (a) 13 and (b) 114 mJ/mm^2.

For the numerically simulated experiments, the lens was located 13 cm above the surface of water. Noise was added to the input transverse beam profile so as to mimic irregularities on the beam profile and start from realistic initial conditions (as close as possible to experimental conditions). Most of the numerical simulations results in this section deal with a comparison of the laser energy deposition in the focal volume when the duration of the input pulses varies from 0.5 ps to 5 ps, while the pulse energy of 290 mJ is kept constant.

Figure 4 represents a comparison of fluence profiles obtained from numerical simulations with initial pulse durations of 0.5 ps and 5 ps at the same pulse energy 290 mJ. Converging multiple filaments are formed in both cases. The shorter initial pulse initiates filament formation earlier in propagation because the initial peak intensity is 10 times larger and filament generation is directly linked to intensity via modulational instability, which has a maximum growth rate proportional to the intensity. The corresponding plasma density profiles are presented in Fig. 5(a,b). The plasma volume is larger for the shorter pulse, however, a closer inspection reveals that the plasma is more localized for the 5 ps pulse, and density reaches slightly higher values.

This result foresees that the heating of water with ps pulses will be more severe. The existence of opti-

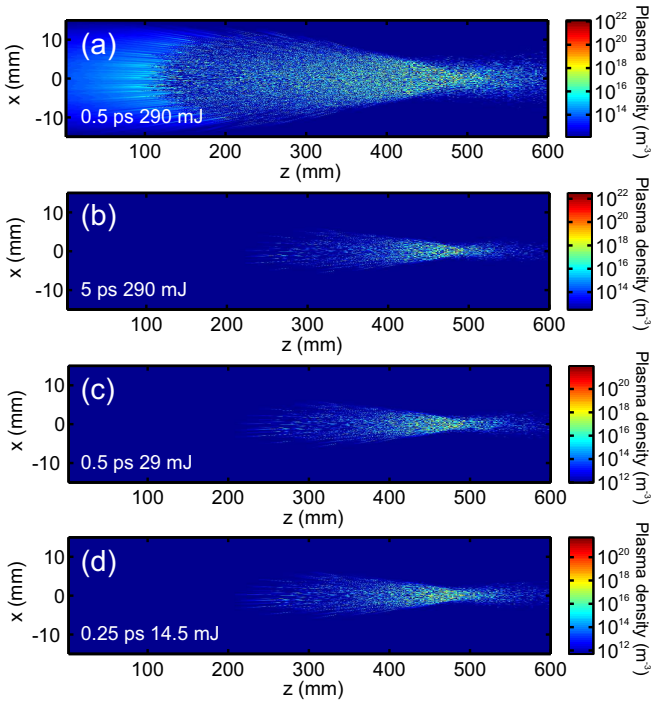


FIG. 5. Plasma density, ρ_e, profiles in the same conditions as in Fig. 4 is depicted in (a) and (b) i.e. when input pulse energy 290 mJ and pulse duration: (a) 0.5 ps; (b) 5 ps. While (b), (c) and (d) are for the cases when input beam peak power was the same for pulse durations 5, 0.5 and 0.25 ps respectively. Maximum plasma densities are 12.4 $\times 10^{21}$, 31×10^{21}, 9.5×10^{21}, 4.9×10^{21} m^{-3} for (a), (b), (c), (d) respectively.

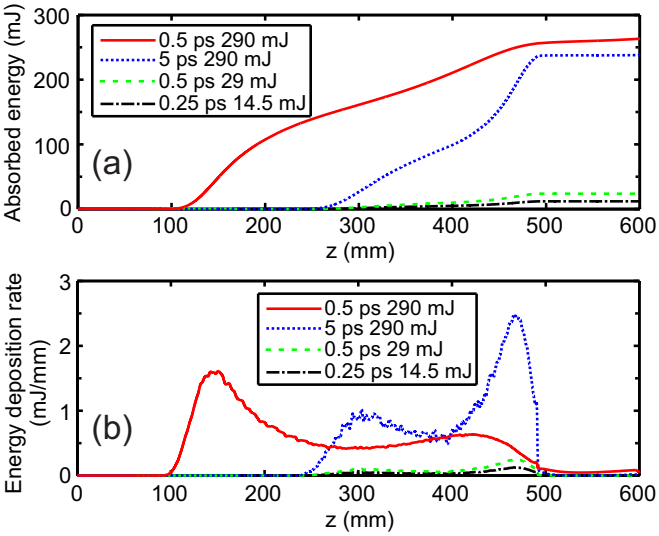


FIG. 6. (a) Absorbed energy, $\langle U \rangle$, and (b) rate of nonlinear energy losses, $\mathrm{d}\langle U \rangle/\mathrm{d}z$, as a function of propagation distance. The curves correspond to different input pulse energies and pulse durations: 290 mJ, 5 ps (dotted blue); 290 mJ, 0.5 ps (solid red), 29 mJ, 0.5 ps (dashed green) and 14.5 mJ, 0.25 ps (dash-dot black). The dotted blue and solid red curves correspond to pulses with the same energy while the dotted blue, dashed green and dash-dot black curves correspond to beams with the same peak power.

mal pulse (of a few ps's) width that maximizes the deposited energy density appears due to local optimization of plasma generation processes (multi photon and avalanche ionization) and beam propagation properties (focusing conditions, self-focusing, plasma defocusing, material dispersion) and is systematically observed in experiments and numerical simulations in dielectrics (see. e.g., [21, 34, 35]). Figures 4 and 5(a,b) compare nonlinear propagation of pulses with the same energy, as in the experiments, resulting in differences in the focal volume mainly due to the different initial peak intensity (power). Figure 5(b,c,d) compares plasma density profiles when the initial peak intensity (peak power) is the same for different initial pulse durations 5 ps, 0.5 ps and 0.25 ps, corresponding to pulse energies of 290, 29 and 14.5 mJ, respectively. In this case the dynamics of multiple filamentation and the features of the plasma volume do not differ significantly. Filaments are generated roughly within the same volume, however, the longest pulse generates plasma at higher density due to a more significant contribution of avalanche ionization.

In order to investigate numerically the propagation of acoustic waves from the focal region to the hydrophone, we analyzed the efficiency of laser energy deposition as a function of pulse duration. Figure 6a shows energy losses for all cases discussed previously without separating multiphoton absorption and plasma absorption as both are contributing to locally heat water. Energy transfer to matter is the most important quantity for evaluating heat increase of the matter. The 0.5 ps and 5 ps pulses deposit 89 % and 82 % of their initial energy (290 mJ), respectively. However 0.5 ps pulse starts to lose energy via ionization of water much earlier than the 5 ps pulse (after propagating 100 mm and 250 mm respectively). By comparing plasma density plots in Fig. 5(a,b) it is evident that the plasma volume is also larger for the 0.5 ps pulse. This suggests that the deposited energy density might be lower for the short pulse. Figure 6a also shows that by shortening the pulse duration while keeping the peak power fixed, energy loss is decreasing while the plasma generation roughly starts at the same position. In order to have a diagnostic of the local rate of energy losses, we calculated the derivative of the absorbed energy $\mathrm{d}\langle U \rangle/\mathrm{d}z$ which represents the energy deposition rate per unit length along the propagation axis

$$\frac{\mathrm{d}\langle U \rangle}{\mathrm{d}z} = \iiint_{-\infty}^{+\infty} u(x,y,z,t)\ \mathrm{d}x\mathrm{d}y\mathrm{d}t, \qquad (1)$$

where the density of nonlinear losses reads

$$u(x,y,z,t) = (\sigma \rho_e I + \beta_K I^K) \times (1 - \rho_e/\rho_{nt}). \qquad (2)$$

Here, σ is the cross section for inverse Bremsstrahlung, $\rho_e(x,y,z,t)$ is the plasma density, I is the intensity associated to the electric field, β_K is the multiphoton absorption (MPA) coefficient, K is the MPA order, and ρ_{nt} is the neutral atom density (see values and further details in Appendix A). The quantity $\mathrm{d}\langle U\rangle/\mathrm{d}z$ is depicted in Fig. 6(b). For the 0.5 ps pulse, the energy deposition rate exhibits a maximum around $z = 15$ cm, at the position where multiple filaments form. However, closer to the focus, the energy deposition rate for the 5 ps pulse is the highest. This result already indicates that long pulses deposit energy closer to the linear focus, while the short pulses generates multiple filaments and looses substantial amount of energy long before they reach linear focus. To evaluate the average energy deposited within the focal volume, we evaluate the deposited energy volume by calculating the second order moment I_2 of deposited energy assuming a super Gaussian shape:

$$I_1 = \iiint_{-\infty}^{+\infty} u(x,y,z,t)\mathrm{d}x\mathrm{d}y\mathrm{d}t = U_m(z)\int_0^{+\infty}\exp\left(-\frac{r^{2s}}{R^{2s}(z)}\right)2\pi r\mathrm{d}r = U_m(z)\pi R^2(z)\Gamma\left(1+\frac{1}{s}\right)$$
$$I_2 = \iiint_{-\infty}^{+\infty}\left(x^2+y^2\right)u(x,y,z,t)\mathrm{d}x\mathrm{d}y\mathrm{d}t = U_m(z)\int_0^{+\infty} r^2\exp\left(-\frac{r^{2s}}{R^{2s}(z)}\right)2\pi r\mathrm{d}r = U_m(z)\frac{\pi}{2}R^4(z)\Gamma\left(1+\frac{2}{s}\right) \quad (3)$$

where Γ denotes the Gamma function. From the numerical evaluation of the deposited energy rate I_1 and the second order moment I_2, we can fully characterize the energy deposition per unit volume, $u_m(r,z)$:

$$u_m(r,z) \equiv U_m(z)\exp\left(-\frac{r^{2s}}{R^{2s}(z)}\right)$$
$$U_m(z) = \frac{I_1^2(z)\Gamma(1+2/s)}{2\pi I_2(z)\Gamma(1+1/s)^2}$$
$$R^2(z) = \frac{2I_2(z)\Gamma(1+1/s)}{I_1(z)\Gamma(1+2/s)}. \quad (4)$$

The radius, $R(z)$, of the energy deposition volume calculated from the distribution of deposited energy is depicted in Fig. 7 by green solid curves. The plasma is not homogeneous in this region, reflecting the hot spots generated by multiple filamentation. A spectral filtering technique was used to characterize energy deposition at the meso-scale level, intermediate between the micro plasma channels and the entire focal volume. Figure 7b shows the locally averaged plasma density obtained through this procedure. Similarly to the phenomenon of superfilamentation in air [29], plasma channels tend to merge and become undistinguishable around the focus, with an average plasma density exceeding that at the entrance of the focal region. This is in line with recent observations [28] of filamentation in water.

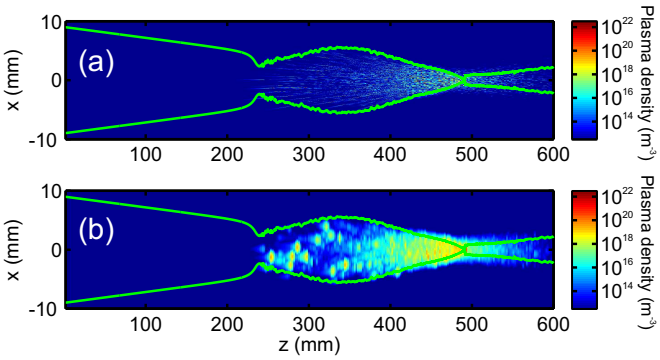


FIG. 7. Plasma density, ρ_e, distribution from the simulation of pulse propagation with initial energy of 290 mJ and duration of 5 ps (a). The solid green curve represents the boundary of the focal (plasma) volume. (b) Spectrally filtered plasma density distribution for the same conditions. A log scale is used for both figures.

The quantitative comparison between the densities of deposited energy, $U_m(z)$, for different cases is depicted in Fig. 8. It is shown that the density of deposited energy is much larger for 5 ps pulses than in any other case. We note that the sound wave can be recorded by the hydrophone only when the amplitude overcomes the noise level set by the dynamic range of the hydrophone. Therefore, by comparing Figs. 3 and 8, we can roughly estimate the deposited energy density threshold that must be reached as to generate an acoustic signal above the detection threshold. By placing this threshold around 40 μJ/mm^3, we immediately observe that shorter pulses ($\lesssim$0.5 ps) produce localized sources for sound waves at the nonlinear focus (where the red (solid), green(dashed), and black (dash-dot) curves overcome this threshold). Therefore for short pulses acoustic waves in the far field will be registered as coming from a point source. On the contrary, longer pulses (5 ps) clearly overcome the 40 μJ/mm^3 threshold over a larger distance (from $z \approx 420$ mm up to $z \approx 500$ mm) and are hence expected to generate sound waves from this extended region. All these observations match qualitatively and quantitatively very well our experimental findings.

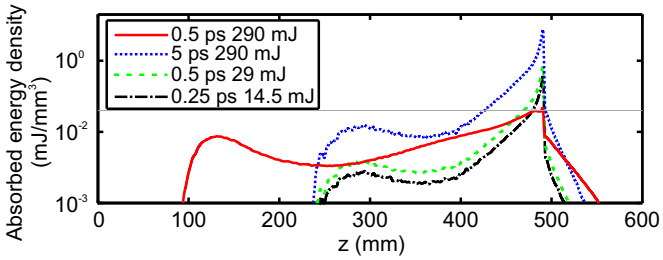


FIG. 8. Absorbed energy density, U_m, versus propagation distance. Different initial beam energies and pulse durations are represented with different colors and are the same as in Fig 6. The thin gray horizontal line represents an approximate threshold value (40 μJ/mm^3) for pressure wave to be registered by the hydrophone (see Fig. 1).

IV. NUMERICAL SIMULATIONS OF ACOUSTIC WAVE GENERATION AND PROPAGATION

In this section we present hydrodynamic simulations showing the propagation of the acoustic waves generated at the laser focus. In all our results below we assume cylindrical geometry with revolution symmetry and therefore rely on the averaged energy deposited distribution $u_m(r,z)$, introduced in Eq. (4), with super-Gaussian order $s = 4$. This distribution is converted into temperature rise by means of the relation (see, e.g., Ref. [36])

$$\Delta T \equiv T(r,z;t=0) - T_0 = \frac{u_m(r,z)}{1.5 k_B \rho_{nt}}, \qquad (5)$$

where $T_0 \approx 300$ K is the fluid equilibrium temperature, k_B the Boltzmann constant, and $\rho_{nt} = 6.7 \times 10^{28}$ m^{-3} is the neutral species number density that corresponds to a mass density of water $\rho_0 \approx 998.2$ kg/m^3. Equation (5) assumes an isochoric (constant volume) heating process which is justified in our case because the pulse transit time ($\lesssim$ps) and the thermalisation time ($\sim$ps) are much shorter than the fluid motion time scales ($\sim$ns). This induces thermal and stress confinement conditions that produce a pressure elevation at the laser focus [37], which results in the formation of acoustic waves through thermo-elasticity effects [38, 39]. The temperature rise calculated from Eq. (5) is converted into the initial pressure field used in all our simulations (see Fig. 9). This is done by means of the relation $p = p(T, \rho_0)$ provided by the Mie-Grüneisen equation of state for water (see Ref. [40] for details). Figure 9 shows the temperature and pressure distributions induced by the laser heating, corresponding to the deposited energy density depicted in Fig. 8 for 5 ps and 290 mJ (blue dotted curve). We note that the procedure of radially averaging the deposited energy leads to a maximum elevation of temperature of ΔT_{max} =6 K above the background, corresponding to a peak pressure of $\sim$9 MPa. We also performed calculations for a higher elevation of temperature ΔT_{max} =70 K, corresponding to a peak pressure of $\sim$100 MPa (see rightmost colorbar in Fig. 9b), to check whether nonlinearity significantly modifies the acoustic wave.

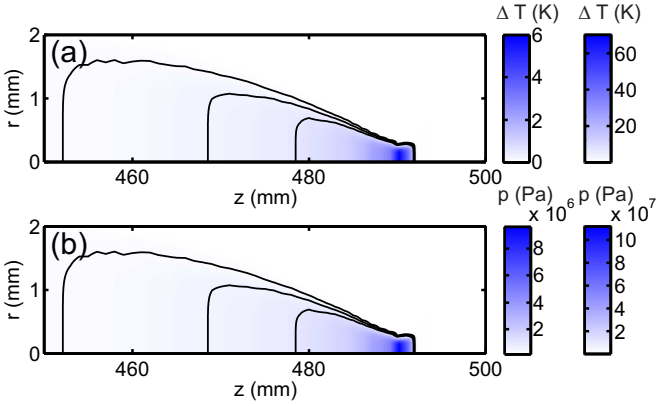


FIG. 9. Initial (a) temperature and (b) pressure distributions for peak heatings of $\Delta T_{max} \equiv \max\{T(r,z,t=0) - T_0\} = 6$ K (leftmost colorbars) and $\Delta T_{max} = 70$ K (rightmost colorbars). The contours are at 1/10, 1/20, and 1/50 of the difference between the maximum and background levels, $p_0 = 1.023 \times 10^5$ Pa (corresponding to a depth of the order of 10 cm in water of background density ρ_0= 998.2 kg/m^3), and $T_0 = 300$ K. Same criterion for contours is applied to Figs. 10 and 11.

In our approach, we have used both linear and nonlinear hydrodynamic models which are presented below.

A. Linear acoustics

In order to interpret the recorded profile of the acoustic signal, we performed simulations of the propagation of acoustic waves by using a simplified model, using the linearized continuity equation and equation of motion for density, ρ_a, and fluid velocity, $\mathbf{v}$,

$$\frac{\partial \rho_a}{\partial t} + \rho_0 \boldsymbol{\nabla} \cdot \mathbf{v} = 0,$$
$$\frac{\partial \mathbf{v}}{\partial t} + \frac{1}{\rho_0} \boldsymbol{\nabla} p_a = 0, \qquad (6)$$

where $p_a = c_s^2 \rho_a$ and $c_s = 1487$ m/s is the speed of sound. We assumed cylindrical symmetry. The subscript a (from *acoustic*) denotes deviations from the equilibrium values, denoted with subscript 0: $\rho_a = \rho - \rho_0$, $p_a = p - p_0$ (note the velocity $\mathbf{v}$ is unambiguously a deviation from equilibrium, $v_0 \equiv 0$, so no subscript is added to it). For a comparison with experimental results, the pressure wave amplitude was calculated at a fixed distance of 5 mm from the source. This distance ensures that the signal propagated far enough from the source to be considered as a far-field measurement, without a need of expanding further the radial coordinate axis (see Appendix B). Results shown below in Fig. 11 (a) clearly exhibit the same structure as the experimental results plotted in Fig. (3) (c). By structure we mean a V-shaped acoustic wave with higher pressure deviations from equilibrium at the

tip whose overpressure (underpressure) is found at its leading (trailing) tail. This indicates that the two acoustic branches measured in Fig. 3 (c) originate from a geometric effect associated with the V-shaped plasma volume, associated to the generation of a converging multifilament bundle that yields the phenomenon of superfilamentation [29]. The geometry of the source of acoustic waves and their linear propagation are sufficient to explain the main features of the signal.

B. Nonlinear hydrodynamics and acoustic wave generation

We have investigated numerically the initial expansion of the focal volume after laser energy deposition in order to check if cavitation and shock wave formation significantly affect the dynamics. To this end we simulate the compressible Euler equations with heat flux,

$$\begin{aligned}
&\frac{\partial \rho}{\partial t} + \boldsymbol{\nabla} \cdot (\rho \mathbf{v}) = 0 \\
&\frac{\partial (\rho \mathbf{v})}{\partial t} + \boldsymbol{\nabla} \cdot (\rho \mathbf{v}\mathbf{v} + p\mathbf{I}) = \mathbf{0} \\
&\frac{\partial e}{\partial t} + \boldsymbol{\nabla} \cdot ([e+p]\mathbf{v} - \lambda \boldsymbol{\nabla} T) = 0, \qquad (7)
\end{aligned}$$

where $e = \rho\epsilon + \frac{1}{2}\rho|\mathbf{v}|^2$ is the total energy per unit volume and $\mathbf{I}$ is the identity matrix. The system of equations above is closed with the additional expressions for the specific internal energy, $\epsilon(\rho, T)$, and pressure, $p(\rho, T)$, given by the equation of state (see Ref. [40]). Here λ=0.58 J(Kms)$^{-1}$ is the heat flux coefficient and T is the temperature. For waves of small amplitude, Eqns. (7) reduce to the linear set given by Eqns. 6 (see Appendix B).

Equations (7) are integrated in time, t, by means of a hyperbolic solver [41]. Figure 10 shows the thermodynamic variables ρ, T, and p 10 μs after the pulse transit. Our simulations are initialized with i) the pressure distribution $p(r, z)$ shown in Fig. 9, ii) the equilibrium density ρ_0= 998.2 kg/m^3 everywhere, fluid at rest iii) $\mathbf{v}(t = 0) = \mathbf{0}$, consistent with ii) because the medium barely moves during the ultrafast isochoric heating process, and iv) with $e(\rho_0, p)$ given by the equation of state.

Figure 10 presents results obtained by assuming initial peak temperatures ΔT_{max} =6 K (left) and 70 K (right) above the room temperature T_0 = 300 K. The initial stages are characterized by a fast evolution of density and pressure. This is due to the ultrafast energy deposition from the laser source to the medium, which occurs at constant density rather than at a constant pressure (i.e, in mechanical equilibrium). Heating of the focal volume occurs while plasma recombines, much faster than the hydrodynamic time-scales for diffusion or fluid motion and therefore the system is driven out of the equilibrium. Immediately after the heating of the focal volume, the temperature remains almost constant in time due to

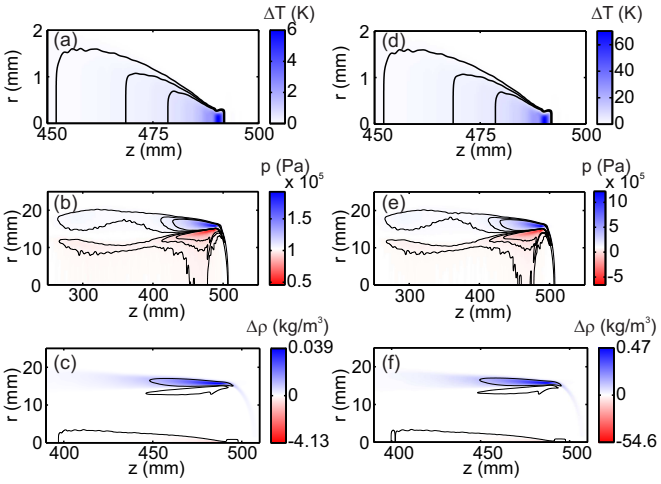


FIG. 10. (a,d) Temperature, ΔT, (b,e) pressure, p, and (c,f) density $\Delta\rho \equiv \rho - \rho_0$, distributions in water 10 μs after the pulse heating. (a-c) ΔT_{max} = 6 K, (d-f) ΔT_{max} = 70 K. ρ_0= 998.2 kg/m^3 and T_0 = 300 K.

the very low heat conductivity (T relaxes over the scale of ms in water). Under these conditions, the density of water rapidly drops below the background level as pressure decreases to restore the mechanical equilibrium (flat p) around the laser focus. This transient process is indeed the responsible for the emission of an acoustic wave. In the far-field, only the amplitude of the acoustic wave differs but the wave profile is similar for both heating levels.

Figure 11 shows a comparison of the temporal profile for the acoustic signals that would be captured by a hydrophone placed 5 mm off axis, for linear and nonlinear simulations initiated with different over-pressures. The lower is the initial overpressure, the closer the agreement is expected to be between Eqns. (7) and (6). However, results are close for heating levels up to 70 K above the background temperature. We observe that the profiles of the acoustic waves simulated with the compressible Euler equations (Figs. 11b,c) are very close to that obtained by linear acoustics (Fig. 11a), and all are in good qualitative agreement with the measured profile (Fig. 3c). These results confirm that the geometry of the source of acoustic waves and their linear propagation are sufficient to explain the main features of the signal. However, this cannot be granted in general (see discussion in Appendix B). Additionally, even a weak localized heating can easily induce cavitation and phase changes. Thus, simulations carried out with the compressible Euler equations allowed us to check that there is little difference in the acoustic wave propagation once it is detached from the focal region. The two branches in the far-field acoustic signal in Fig. 2 originate essentially from the shape of the plasma volume where laser energy is deposited.

We note from Figs. 10(e) and Figs. 11(b,c), the negative pressure (or tension) tail that travels attached to the pressure wave. These negative values disappear dur-

ing the first couple of μs. In none of our simulations, the system was ever close to the Kinetic spinodal, defined by *S. B. Kiselev* [42]. In particular, for our most extreme simulations ($\Delta T_{max} = 70$ K) the minimum achieved pressure value is $p = -55$ MPa, which is well above the Kinetic spinodal boundary located at around -100 MPa (for temperatures of 300-370 K) [43]. Therefore no spinodal decomposition effects [44] needed to be included in our cases and all negative pressure values correspond to water in the meta-stable state [44, 45]. Therefore, consistently with the definition of Kiselev's spinodal [42], the lifetimes of the meta-stability are expected to be substantially longer than those of the relaxation of the system towards the equilibrium, which is simply driven, in our case, by the hydrodynamic motion described by Eqns. 7. We note that this same criterion is commonly used in the literature as to identify the onset of cavitation (see, e.g., Refs. [37, 46, 47]).

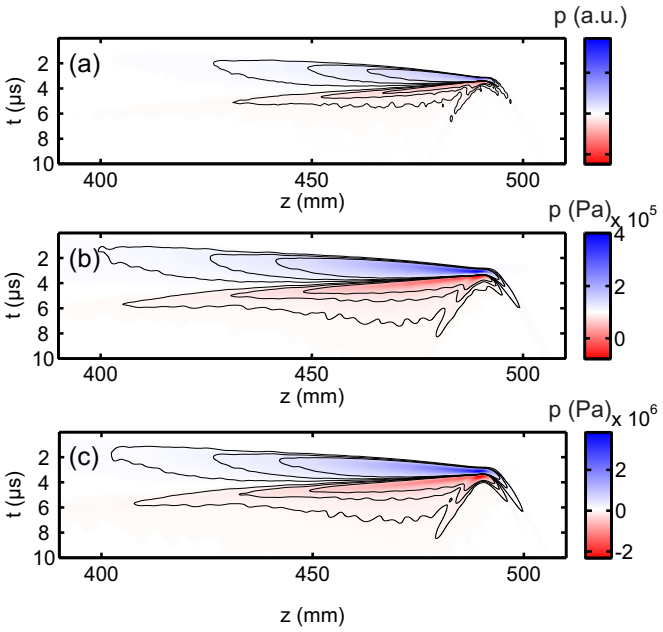


FIG. 11. Simulated pressure vs time signal recorded at an offset of 5 mm from the pulse propagation axis, z. Simulations show (a) linear (Eqns. 6) and (b,c) nonlinear (Eqns. 7) calculations, the latter for (b) $\Delta T_{max} = 6$ K and (c) $\Delta T_{max} = 70$ K.

In our numerical simulations we have let the water be in the metastable state because it did not reach the homogeneous nucleation threshold (as explained above). In this way we have neglected effects introduced by heterogeneous nucleation, i.e., the lower threshold cavitation taking place due to the presence of impurities in liquids. Adding heterogeneous nucleation in a continuum model like Eq. 7 would require making assumptions about the density and size distribution of nuclei (see, e.g., Ref. [48]), and considering, e.g., a distribution of oscillating bubbles coupled with the continuum model. This would allow for describing how these oscillators (bubbles) grow and possibly coalesce with each other, and how this would modify the acoustic waves but goes beyond the scope of this work. The good agreement we found with experiments by only considering the homogeneous nucleation barrier as well as data provided in previous works on this topic qualitatively backs up our assumption. For example, Ref. [49] demonstrates that stresses of ~ 10 MPa in impure water exerted during times of ~ 1 μs do not induce cavitation and therefore heterogeneous nucleation can be dismissed for stresses below this threshold, which is comparable to the order of magnitude of stresses we calculated.

We also performed a numerical directivity study. We recorded pressure vs time on 300 virtual microphones evenly distributed over the 50 mm radius half circumference centered at the position of the maximum initial pressure ($r = 0$, $z \approx 490$ mm). In Figs.12(a-c) a comparison between the numerical (blue (gray)) and experimental (black) results is shown for the angular dependence of the amplitude for selected frequencies. We attribute the discrepancy in between simulations and experiments at low frequencies to the closer position of microphones used in the numerical simulations. Figure 12(d) shows the spectrally integrated directivity. At the distances of tens of centimetres (5 cm for simulations, 38 cm for experiments), most of the sound wave energy is distributed perpendicularly to the beam propagation axis, as measured and shown by Y. Brelet et al. [13]. We note that the directivity is sharply peaked for higher frequencies. This is directly related to the geometrical features of the acoustic source. On the one hand, the thin (~ 100 μm) high peak pressure distribution at $z \sim 490$ mm generates acoustic waves with relatively steep fronts and short wavelengths (higher carrier frequencies). Because this region of the source is predominantly oriented along the z-axis the waves are predominantly emitted in the radial direction (around $\theta \approx 90°$). On the other hand, the much larger and dellocalized volume of the conically shaped initial pressure profile (i.e., the lower pressure region around $z \sim 450 - 480$ mm) generates smoother acoustic waves with longer wavelengths (lower frequencies) emitted sparser, so the directivity is looser.

In practice, if one aims at using this type of sources for communication or detection in the range of 10s of meters, then the damping of the different frequencies in the acoustic signal becomes important. We have taken into account the chromatic losses of pure water (cf. Ref. [50]) and performed estimates of the spectrally integrated directivity at longer distances from the source. In Fig. 12(d) we show the effect of losses at 10 m (dotted) and 100 m (dashed) away from the source. The quadratic dependence of losses with frequency strongly damps the higher frequencies of the waves (losses are about 45, 720, 3600 dB/km for 0.5, 2, 4.5 MHz, respectively). The survival of the lower frequency components notably broadens the directivity, whose maximum is now found at $\theta \approx 100°$, but in overall the directivity remains relatively high.

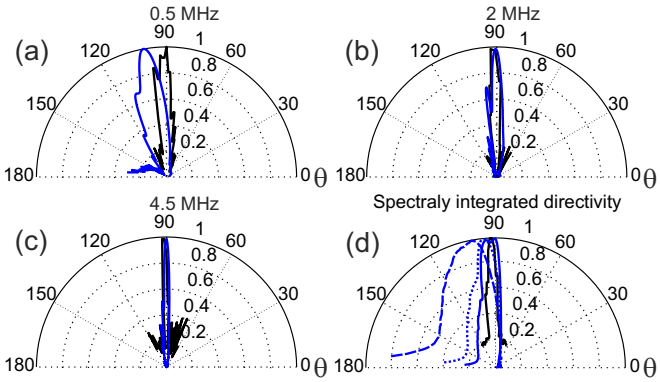


FIG. 12. Sound wave directivity measured from experiments (from Ref.[13], black curves) and numerical simulations with $\Delta = 70$ K (at 50 mm from the source, blue (gray) curves) for (a) 0.5 MHz, (b) 2 MHz, and (c) 4.5 MHz. The maximum pressure recorded numerically at this distance is of 2 MPa above the background ~ 0.1 MPa and the maximum amplitudes for the selected frequencies correspond to (a) 5.3×10^5 Pa/MHz, (b) 2.88×10^5 Pa/MHz, and (c) 0.98×10^5 Pa/MHz. (d) Shows spectrally integrated angular distributions corresponding to distances of 38 cm (solid blue (gray)), 10 m (dotted), and 100 m (dashed) away from the source. In (d), directivity plots are scaled to 1, and the relative ratios are 0.57 (10 m to 38 cm) and 0.22 (100 m to 38 cm). In all figures, θ is measured from the z axis: 0° (180°) corresponds to the forward (backward) laser propagation direction.

V. CONCLUSION

We have demonstrated a high directivity acoustic source generated by loosely focused multi millijoule picosecond pulses in water. The acoustic wave predominantly propagates transversally to the laser beam and its origin is attributed to the phenomenon of superfilamentation. The dependence of the acoustic signal upon pulse duration is numerically and experimentally investigated. While fs pulses tend to produce a point acoustic source and energy deposition per unit volume remains relatively low, ps pulses produce an extended source and deposit much more energy per unit volume, yielding very high directivity and higher power. The laser induced hydrodynamics is fully studied numerically by means of the compressible Euler equations and a suitable equations of state for water. Additionally, a simplified linear acoustic model provides efficient calculations of the pressure far fields, linking the calculations with the experimental measurements. The combination of optical and hydrodynamical results are in an overall good agreement with experiments. Our findings are relevant for underwater detection and communications, where the ability to dynamically control the directivity of the acoustic sources is important.

ACKNOWLEDGMENTS

This project has been supported by the French Direction Generale de l'Armement (Grant numbers 066003600470750, 2012.60.0013 and 2015.60.0004). The authors thank the staff from Laboratoire de Mecanique et Acoustique for technical assistance.

Appendix A

The propagation equation used for laser beam filamentation:

$$\frac{\partial E}{\partial z} = \frac{i}{2n_0k_0}\nabla_\perp^2 E + ik_0n_2|E|^2E - \frac{\sigma}{2}(1+i\omega_0\tau_c)\rho_e E - \frac{\beta_K}{2}|E|^{2K-2}\left(1-\frac{\rho_e}{\rho_{nt}}\right)E,$$
$$\frac{\partial \rho_e}{\partial t} = \left(\frac{\beta_K}{K\hbar\omega_0}|E|^{2K} + \frac{\sigma}{U_i}\rho_e|E|^2\right)\left(1-\frac{\rho_e}{\rho_{nt}}\right). \quad \text{(A1)}$$

Here, n_0=1.33 is the refractive index at $\lambda_0 = 800$ nm, n_2=1.9×10^{-16} cm^2/W is the nonlinear refractive index, $\sigma \equiv \omega_0^2\tau_c[n_0c\rho_c(1+w_0^2\tau_c^2)]^{-1} \approx 4.7\times10^{-22}$ m^2 is the cross section for inverse Bremsstrahlung [51], where τ_c=3 fs is the electron collision time, β_K=8.3×10^{-52} cm^7/W^4 is the multiphoton absorption (MPA) coefficient, K=5 is MPA order, U_i=6.5 eV is the ionisation potential [52], ρ_{nt}=6.7×10^{22} cm^{-3} is the neutral atom density, ρ_e the plasma density and $\rho_c \equiv \omega_0^2 m_e\epsilon_0/e^2 \approx 1.7\times10^{21}$cm^{-3} its critical value (m_e, ϵ_0, and e are the electron mass, vacuum permittivity, and elementary charge, respectively). The choice of τ_c and β_K is taken from Ref. [21], where a good quantitative comparison between experiments and numerical simulation was achieved (albeit for much lower pulse energies). We note the maximum levels of intensity reached in our simulations give a Keldysh parameter $\gamma \sim 4$ and therefore we are very much below the tunnelling ionisation threshold. In this situation the full Keldysh rate and the MPA rate ($\propto \beta_K I^K$) used by us are almost equivalent.

Appendix B

Here we show explicitly that our hydrodynamic simulations based on Euler equations (7) become quasi-linear after the acoustic waves detach from the laser focus and propagate only a few millimeters away from the z axis. Therefore, the evolution at longer distances (needed to produce the results presented in Fig. 12) can be calculated by the simpler (and numerically faster) linear system of Eqns. (6). We first note that, by following the standard procedure in Ref.[53], the energy equation in Eqns. (7) may be replaced for that of specific entropy, s,

so the system of equations reads:

$$\frac{\partial \rho}{\partial t} + \boldsymbol{\nabla} \cdot (\rho \mathbf{v}) = 0$$
$$\frac{\partial (\rho \mathbf{v})}{\partial t} + \boldsymbol{\nabla} \cdot (\rho \mathbf{v}\mathbf{v} + p\mathbf{I}) = \mathbf{0}$$
$$\rho T \left(\frac{\partial s}{\partial t} + \mathbf{v} \boldsymbol{\nabla} s \right) - \boldsymbol{\nabla} (\lambda \boldsymbol{\nabla} T) = 0. \quad \text{(B1)}$$

Rewriting the above system for the deviation from equilibrium of all thermodynamic quantities, x_0 (density, pressure, entropy, etc.), i.e., applying the transformation $x \to x_0 + x_a$, where x_a are now offsets from equilibrium, we obtain

$$\frac{\partial \rho_a}{\partial t} + \rho_0 \boldsymbol{\nabla} \cdot \mathbf{v} = -\rho_a \boldsymbol{\nabla} \cdot \mathbf{v} \quad \text{(B2a)}$$
$$\frac{\partial \mathbf{v}}{\partial t} + \frac{1}{\rho_0} \boldsymbol{\nabla} p_a \approx \mathbf{v} (\boldsymbol{\nabla} \cdot \mathbf{v}) - \boldsymbol{\nabla} \cdot \left(\frac{\rho_a}{\rho_0} \mathbf{v}\mathbf{v} \right) \quad \text{(B2b)}$$
$$\rho T \left(\frac{\partial s_a}{\partial t} + \mathbf{v} \boldsymbol{\nabla} s_a \right) = \boldsymbol{\nabla} (\lambda \boldsymbol{\nabla} T_a), \quad \text{(B2c)}$$

where all higher order terms are gathered in the right hand side (RHS) and p_a is given by

$$p_a \approx c_s^2 \rho_a + \left(\frac{\partial p}{\partial s} \right)_\rho s_a, \quad \text{(B3)}$$

where $c_s \equiv \partial p / \partial \rho|_s$. From the above equation it is clear that when the thermodynamic derivative $(\partial p / \partial s)_\rho$ is small, p_a is not a function of s_a so the mass and velocity equations (B2a, B2b) decouple from the entropy equation (B2c). If, additionally, fluid velocities are low ($|\mathbf{v}| \ll c_s$) then Eqns. (B2a,b-B3) indeed reduce to Eqns. (6) with $p_a = c_s^2 \rho_a$. To illustrate this, we consider the acoustic wave in our simulations carried out by means of Eqns.(7) and $\Delta T_{max} = 70$ K up to 10 μs after the laser heating, corresponding to the results presented in Figs. 10(d-f). In the region where the acoustic wave is, density and temperature deviate form equilibrium by around 0.5 kg m^{-3} and 0.15 K, respectively. This means that $\rho_a / \rho_0 \sim 10^{-4}$ and the RHS of eq. (B2a) becomes negligible. Additionally, the dominant term on the RHS of eq. (B2b) $|\mathbf{v}(\boldsymbol{\nabla} \cdot \mathbf{v})| \sim 8 \times 10^2$ m^{2}s$^{-2} \ll |\boldsymbol{\nabla} p_a / \rho_0| \sim 3 \times 10^6$m^{2}s^{-2}, so the RHS is negligible and Eq.(B2b) becomes linear as well. Finally, we use the Mie-Grüneisen equation of state in Ref. [40] to make the following evaluations: $c_s^2 \rho_a \sim 10^6$ Pa, $(\partial p / \partial T)_\rho \sim 1.6 \times 10^6$ Pa, and $(\partial \epsilon / \partial T)_\rho \approx 3270$ J kg^{-1}K^{-1} (specific heat capacity at constant volume). With this, the terms in the RHS of Eq.(B3) become, respectively:

$$c_s^2 \rho_a \approx 2.3 \times 10^6 \text{ Pa}$$
$$\left(\frac{\partial p}{\partial s} \right)_\rho s_a = \left(\frac{\partial p}{\partial T} \right)_\rho T_a - \frac{T_0}{\rho_0^2} \left(\frac{\partial p}{\partial T} \right)_\rho^2 \left(\frac{\partial \epsilon}{\partial T} \right)_\rho^{-1} \rho_a \approx 10^5 \text{ Pa}$$

Hence, the approximation $p_a = c_s^2 \rho_a$ becomes reasonable and, as a result of this, Eqns. (7) may be approximated by Eqns. (6).

[1] M.Versluis, B. Schmitz, A. von derHeydt, and D. Lohse, Science **289**, 2114 (2000).
[2] W. Lauterborn and A. Vogel, *Bubble Dynamics and Shock Waves*, Vol. 8 (Springer-Verlag, Berlin, 2013) pp. 67–103.
[3] W. Lauterborn and T. Kurz, Rep. Prog. Phys. **73**, 106501 (2010).
[4] N. Linz, S. Freidank, X.-X. Liang, H. Vogelmann, T. Trickl, and A. Vogel, Phys. Rev. B **91**, 134114 (2015).
[5] G. A. Askaryan, A. M. Prokhorov, G. F. Chanturiya, and G. P. Shipulo, Sov. Phys. JEPT **44(6)**, 2180 (1963).
[6] R. M. White, J. Appl. Phys. **34(12)**, 3559 (1963).
[7] S. V. Egerev, Acoust. Phys. **49**, 51 (2003).
[8] N. Chotiros, ed., *Proc. SPIE*, Vol. 0925 (1988).
[9] F. Blackmon and L. Antonelli, Appl. Opt. **44**, 103 (2005).
[10] J. Noack and A. Vogel, IEEE J. Quantum Electron. **35**, 1156 (1999).
[11] A. Vogel, J. Noack, K. Nahen, D. Theisen, S. Busch, U. Parlitz, D. X. Hammer, G. D. Noojin, B. A. Rockwell, and R. Birngruber, Appl. Phys. B **68**, 271 (1999).
[12] F. V. Potemkin, E. I. Mareev, A. A. Podshivalov, and V. M. Gordienko, Laser Phys. Lett. **11**, 106001 (2014).
[13] Y. Brelet, A. Jarnac, J. Carbonnel, Y.-B. André, A. Mysyrowicz, A. Houard, D. Fattaccioli, R. Guillermin, and J.-P. Sessarego, J. Acoust. Soc. Am. **137**, EL288 (2015).
[14] A. Couairon and A. Mysyrowicz, Phys. Rep. **441**, 47 (2007).
[15] A. Dubietis, A. Couairon, E. Kučinskas, G. Tamošauskas, E.Gaižauskas, D. Faccio, and P. D. Trapani, Appl. Phys. B **84**, 439 (2006).
[16] S. Minardi, A. Gopal, M. Tatarakis, A. Couairon, G. Tamošauskas, R. Piskarskas, A. Dubietis, and P. D. Trapani, Opt. Lett. **33**, 86 (2008).
[17] S. Minardi, A. Gopal, A. Couairon, G. Tamošauskas, R. Piskarskas, A. Dubietis, and P. D. Trapani, Opt. Lett. **34**, 3020 (2009).
[18] S. Sreeja, C. Leela, V.R.Kumar, S. Bagchi, T. S. Prashant, P. Radhakrishnan, S. P. Tewari, S. V. Rao, and P. P. Kiran, Laser Phys. **23**, 106002 (2013).
[19] A. Jarnac, G. Tamošauskas, D. Majus, A. Houard, A. Mysyrowicz, A. Couairon, and A. Dubietis, Phys. Rev. A **89**, 033809 (2014).
[20] S. Minardi, C. Milián, D. Majus, A. Gopal, G. Tamošauskas, A. Couairon, T. Pertsch, and A. Dubietis, Appl. Phys. Lett. **105**, 224104 (2014).
[21] C. Milián, A. Jarnac, Y. Brelet, V. Jukna, A. Houard, A. Mysyrowicz, and A. Couairon, J. Opt. Soc. Am. B **31**, 2829 (2014).
[22] S. Chin and S. Lagacé, Appl. Opt. **335**, 907 (1996).

[23] D. Faccio, G. Tamošauskas, E. Rubino, J. Darginavičius, D. G. Papazoglou, S. Tzortzakis, A. Couairon, and A. Dubietis, Phys. Rev. E **86**, 036304 (2012).

[24] D. Faccio, E. Rubino, A. Lotti, A. Couairon, A. Dubietis, G. Tamošauskas, D. G. Papazoglou, and S. Tzortzakis, Phys. Rev. A **85**, 033829 (2012).

[25] T. G. Jones, A. Ting, J. Penano, P. Sprangle, and G. DiComo, eds., *Conference on Lasers and Electro-Optics/Conference on Quantum Electronics and Laser Science* (2006) in CThA1.

[26] T. Jones, A. Ting, J. Peñano, P. Sprangle, and L. Bibee, *Remote Intense Laser Acoustic Source*, Tech. Rep. (DTIC Document, 2007).

[27] C. Milián, V. Jukna, A. Couairon, A. Houard, and A. Mysyrowicz, in *The European Conference on Lasers and Electro-Optics* (Optical Society of America, 2015) p. CD_P_3.

[28] F. V. Potemkin, E. I. Mareev, A. A. Podshivalov, and V. M. Gordienko, New J. Phys. **17**, 053010 (2015).

[29] G. Point, Y. Brelet, A. Houard, V. Jukna, C. Milián, J. Carbonnel, Y. Liu, A. Couairon, and A. Mysyrowicz, Phys. Rev. Lett. **112**, 223902 (2014).

[30] C. Milián, V. Jukna, A. Couairon, A. Houard, B. Forestier, J. Carbonnel, Y. Liu, B. Prade, and A. Mysyrowicz, J. Phys. B: At. Mol. Opt. Phys. **48**, 094013 (2015).

[31] I. Dicaire, V. Jukna, C. Praz, C. Milián, L. Summerer, and A. Couairon, Laser Photon. Rev. **10**, 481 (2016).

[32] A. Couairon, E. Brambilla, T. Corti, D. Majus, O. de J. Ramirez-Gongora, and M. Kolesik, Eur. Phys. J.: Spec. Top. **199**, 5 (2011).

[33] E. A. Sziklas and A. E. Siegman, Appl. Opt. **14**, 1873 (1975).

[34] S. Onda, W. Watanabe, K. Yamada, K. Itoh, and J. Nishii, J. Opt. Soc. Am. B **22**, 2437 (2005).

[35] M. K. Bhuyan, P. K. Velpula, J. P. Colombier, T. Olivier, N. Faure, and R. Stoian, Appl. Phys. Lett. **104**, 021107 (2014).

[36] E. Gamaly, Phys. Rep. **508**, 91 (2011).

[37] A. Vogel, J. Noack, G. Hüttman, and G. Paltauf, Appl. Phys. B **81**, 1015 (2005).

[38] G. Paltauf and P. E. Dyer, Chem. Rev. **103**, 487 (2003).

[39] G. Paltauf and H. Schmidt-Kloiber, Appl. Phys. A **68**, 525 (1999).

[40] I. Akhatov, O. Lindau, A. Topolnikov, R. Mettin, N. Vakhitova, and W. Lauterborn, Phys. Fluids **13**, 2805 (2001).

[41] E. F. Toro, M. Spruce, and W. Speares, Shock waves **4**, 25 (1994).

[42] S. Kiselev, Phys. A **269**, 252 (1999).

[43] S. Kiselev and J. Ely, Phys. A **299**, 357 (2001).

[44] V. P. Skripov, *Metastable liquids* (Wiley, 1974).

[45] P. G. Debenedetti, *Metastable liquids: concepts and principles* (Princeton University Press, 1996).

[46] A. Vogel, N. Linz, S. Freidank, and G. Paltauf, Phys. Rev. Lett. **100**, 038102 (2008).

[47] K. Franjic and R. D. Miller, Phys. Chem. Chem. Phys. **12**, 5225 (2010).

[48] M. Strauss, Y. Kaufman, M. Sapir, P. A. Amendt, R. A. London, and M. E. Glinsky, J. Appl. Phys. **91**, 4720 (2002).

[49] J. Staudenraus and W. Eisenmenger, Ultrasonics **31**, 267 (1993).

[50] M. A. Ainslie and J. G. McColm, J. Acoust. Soc. Am. **103**, 1671 (1998).

[51] E. Yablonovitch and N. Bloembergen, Phys. Rev. Lett. **29**, 907 (1972).

[52] P. K. Kennedy, IEEE J. Quant. Electron. **31**, 2241 (1995).

[53] L. Landau and E. M. Lifshitz, *Theoretical Physics. Vol. 6. Hydrodynamics* (Nauka, Moscow, 1986).